

Lunar References Systems, Frames and Time-scales in the context of the ESA Programme Moonlight

Agnès Fienga^{1,2*}, Nicolas Rambaux^{1,2} and Krzysztof Sośnica³

¹Geoazur, Observatoire de la Côte d'Azur, Av. A. Einstein, Sophia-Antipolis, 06560, France.

²IMCCE, Observatoire de Paris, Av. Denfert-Rocheau, Paris, 75014, France.

³Institute of Geodesy and Geoinformatics, Wrocław University of Environmental and Life Sciences, Norwida 25, Wrocław, 50-375, Poland.

*Corresponding author(s). E-mail(s): agnes.fienga@oca.eu, nicolas.rambaux@imcce.fr;

Abstract

Lunar reference systems represent a fundamental aspect of lunar exploration. This paper presents a review of the topic in the context of the ESA lunar programme, MoonLight. This paper describes the current state of the art in the definition of the lunar reference frame and introduces TCL, a lunar time scale based on IAU resolutions. It also proposes several possible implementations of this time scale for orbiting and ground-based clocks. Finally, it provides an assessment of the improvement of the lunar reference frame that would result from the addition of lunar retro-reflectors on the Moon's surface and the use of orbiter altimetry. This document is an appendix dedicated to lunar reference system definition of a more global document dedicated to the presentation of new concepts in orbit determination and time synchronization of a lunar radio navigation system.

Contents

1	State-of-the-art	3
1.1	Introduction	3
1.2	Inertial and Kinematically non-rotating systems	4
1.3	Principal axis (PA) system	4
1.4	Mean Earth direction and rotation system	4
1.5	Semi-analytical series representation	5
1.6	Lunar Laser Ranging Retroreflector as lunar point control	6
2	Proposition of lunar reference systems: the LCRS and the LRS	7
2.1	The Moon-centered inertial Lunar Reference system, LCRS	7
2.1.1	Definition of the metric	7
2.1.2	Definition of the Lunar Time-scale	9
2.1.3	Transformation between BCRS and LCRS	10
2.1.4	Accuracy assessments of the realization	11
2.2	The lunar body-fixed reference system, LRS	11
2.2.1	Comparisons between ephemerides	13
2.2.2	Propagation of the covariance matrix	13
2.2.3	Impact of reference frame on gravity field and orbit computations	14
2.2.4	Link to LRO DTM	18
2.2.5	LRS Time-scales	19
3	Simulations for future improvements	21
3.1	Improvements with additional reflectors	21
3.2	Improvements with MoonLight altimetry	25

In response to the recent need of space agencies to develop new capabilities of robust navigation and positioning infrastructure to support the numerous Moon missions planned for the mid-term future, ESA has established the programme Moonlight [8], for the development of a reliable yet simple lunar communication and navigation service (LCNS). The fundamental elements of such a system are a precise definition of the reference frames and time scales, accurate satellite ephemerides, synchronisation of time across the constellation and with the ground control centre, stable onboard clocks and the construction of one-way radio signals to be delivered to the end user together with a precise navigation message. New concepts for achieving Moonlight goals have been proposed by [9], in a work, funded by ESA, and carried out by a consortium (named ATLAS) that exploited synergies between academic institutions and industries in Europe. The present document is the appendix of this work dedicated to lunar reference definition.

1 State-of-the-art

1.1 Introduction

The definition of a lunar body-fixed coordinate system is essential to locate a point on its surface and to establish accurate cartography. These two objectives are particularly crucial in the context of lunar exploration. Moreover, with the deployment of future lunar constellations, the need of a Moon-centered inertial reference system is also increasing with the intensification and the improvement of the orbit determination of artificial satellites orbiting the Moon.

At present, two slightly different reference systems attached to the Moon are commonly used to define the lunar body-fixed coordinate system: the Mean Earth-/Rotation Axis (or polar axis) (ME) reference system and the principal axis (PA) reference system [1, 27]. The former has been used at the beginning of lunar observation and it is commonly adopted for archiving and data distribution proposes of lunar surface or topography. The latter corresponds to the orientation where the lunar tensor of inertia is diagonal. The transformation between the two reference systems is realised by three static Euler angles that depend on the lunar gravity field coefficients and dissipative models. Consequently, this transformation is dependent to a lunar ephemeris. These two coordinate systems are available in the SPICE kernels in PCK format containing high-accuracy and the systems are defined through the TF kernel files [13]. Time-varying Euler angles as defined in section 4.9.2 are also provided with the calceph library.

In preparation of the NASA GRAIL mission (2011-2012), three working groups including the Lunar Geodesy and Cartography Working Group (LGCWG) [13] had proposed to adopt the ME 421 as a reference body-fixed system for the future scientific data archiving, operations, and communication [13].

Finally, in terms of Moon-centered inertial reference system required for the integration of the orbiter equations of motion, no specific system is yet defined by the community but some have been proposed as, for example, by [23] in the context of the GRAIL mission. They are usually the direct adaptation to the Moon of the GCRS system defined by the IAU [21, 19].

1.2 Inertial and Kinematically non-rotating systems

Moon-centered inertial reference systems are necessary for the orbit determination of spacecraft orbiting the Moon. Current definitions of inertial systems are based on the IAU B3 recommendations [21, 19] and the relativistic descriptions of the BCRS and the GCRS based on [2]. The BCRS metric is taken to be kinematically fixed with respect to distant quasi stellar objects (QSO), as defined by [21] and following harmonic gauge conditions. A kinematically non-rotating reference system centered on the Earth center of mass has been defined in the same type of framework, leading to the definition of the Geocentric Celestial Reference System (GCRS). Time-scales derived from the BCRS and the GCRS metric are also given in [21].

For the Moon, [23] had proposed to adapt the GCRS definition to the Moon in the context of the GRAIL mission. A description of such a Moon-centered inertial system is given in Sect. 2.1 with a definition of the Moon centered metric (Sect. 2.1.1) and time-scale (Sect. 2.1.2). In Sect. 2.1.4, an assessment of the accuracy of two possible realisations of LCRS is given by comparing results obtained with DE421 [6] and INPOP19a [4].

1.3 Principal axis (PA) system

The PA system is defined by the principal axis orientation of the inertia matrix of the Moon with constant tides contributions. Indeed, this is a useful reference system to write and to integrate the rotational equation. Its materialisation is realized from the temporal series of the Moon orientation, coming from ephemerides, and described through the rotation Euler angles (ψ precession angle, θ nutation angle, and ϕ proper rotation). The rotational angles are extracted from the lunar ephemerides as for example, the JPL ephemerides DE, or the IMCCE/OCA INPOP. These two ephemerides are similar in terms of weighted root mean square residuals. Let I be a vector in LCRF and PA a vector in the principal-axis reference frame, and R_x and R_z elementary rotational matrices. The transformation is written as [6]

$$PA = R_z(\varphi) R_x(\theta) R_z(\psi) I \quad (1)$$

The inverse transformation is:

$$I = R_z(-\psi) R_x(-\theta) R_z(-\varphi) PA \quad (2)$$

1.4 Mean Earth direction and rotation system

Due to the fact that the Moon is not purely triaxial ellipsoid, the average orientation of the PA does not coincide with the mean Earth direction. The Figure 1 shows the position of the Earth in the Lunar PA reference system over 1 and 6 years. The loops describe the geometrical libration of the Moon. The average of the loops is not exactly zero and there is a constant offset.

The Mean Earth/Polar Axis (ME) reference system is defined by the z -axis as the mean rotational pole. The Prime Meridian (0° Longitude) is defined by the mean Earth direction. The intersection of the lunar Equator and Prime Meridian occurs at

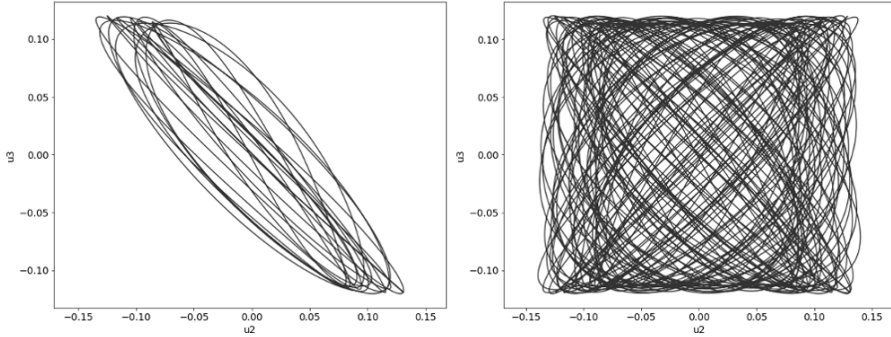


Fig. 1 Direction to Earth from the Moon for 1 year (as) and 6 years. (u_1, u_2, u_3) are cosine of the direction vector of the Earth seen in PA reference frame of the Moon. No units.

Table 1 Numerical values of offset angles for some ephemerides. ((a,b) [27],[20], (c) [17], (d) (Rambaux et al., in progress)).

DE421 (a,b)	-78.513''	0.290''	-67.753''
DE440 (c)	-78.694''	0.278''	-67.853''
INPOP19a (d)	-78.594''	0.290''	-67.930''

what can be called the Moon’s “mean sub-Earth point”. This system is an idealization; a practical attempt to determine these mean directions with high accuracy would depend on the approach and time interval used. This reference system is defined from the numerical ephemerides of the PA system through the following rotation matrix relationship [6]

$$ME = R_x(-p_{2c})R_y(p_{1c})R_z(-\tau_c + I_c^2 \frac{\sigma_c}{2})PA \quad (3)$$

where I_c is the Moon moment of inertia, p_{1c}, p_{2c} , are constant coordinates of ecliptic pole in PA reference frame, while τ_c and σ_c are constant libration angles. The offset between these coordinate systems of a point on the lunar surface is approximately 860 meters and depends on the ephemeris and on the gravity field associated. Table 1 reports two examples with DE and preliminary solution for INPOP.

In this case, the inverse transformation is:

$$I = R_z(-\psi)R_x(-\theta)R_z(-\varphi)R_z\left(\tau_c - I_c^2 \frac{\sigma_c}{2}\right)R_y(-p_{1c})R_x(+p_{2c})ME \quad (4)$$

1.5 Semi-analytical series representation

The IAU WG provided until 2013 the right ascension, declination of the lunar north pole and the prime meridian from proper rotation angle using time series. This representation has been stopped in [1] because this is less accurate (< 150 m) than numerical procedure [10]. Such representation is more compact than the Chebychev polynomial representation and, if useful, it is possible to expand the representation to a desire accuracy through ephemerides such as INPOP.

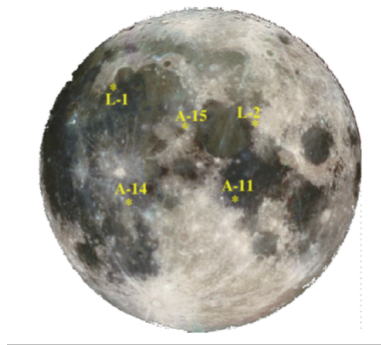


Fig. 2 Location of the LLRR at the Moon surface.

Table 2 Maximum differences in LLRR positions between INPOP17a [25], INPOP19a [4], INPOP21a [5], EPM [18], DE421 [6], DE440 [17].

LLRR	INPOP17a- INPOP21a [m]	EPM- INPOP17a [m]	INPOP21a- DE421 [m]	INPOP21a- DE440 [m]	INPOP19a- INPOP20a [m]
Apollo 11	0.108	2.3	1.361	0.898	0.078
Apollo 14	0.101	2.2	1.601	0.838	0.051
Apollo 15	0.148	2.2	1.409	1.030	0.091
Lunokhod 1	0.249	2.2	-	0.837	0.083
Lunokhod 2	0.186	1.9	1.156	0.949	0.061

1.6 Lunar Laser Ranging Retroreflector as lunar point control

There are five particular points on the Moon whose positions are very well measured. They are the Lunar Laser Ranging Retroreflector (LLRR) and their distribution is shown in Figure 2 and they can be used as lunar control point network.

The stability of the LLRR positions has been discussed recently in [28] who computed the coordinate rates of LLRR. The weighted average rate of four LLR is 8.3 ± 3.1 mm/year, so 20 cm in 25 years. The origin of this shift is not known but they argued that it could be due to mismodelling in rotational motion. Figure 3 illustrates the differences in positions of the LLRR for different ephemerides.

Finally, the formal uncertainties in the positions of the LLRR is about 3 cm in INPOP and the global uncertainty in positions is 40 cm for DE [27]. These uncertainties of few 10s of centimeters represent the internal precision in ephemerides. The comparison of various ephemerides as in Table 2 provides the external accuracy that is about 2 meters for EPM [18] vs DE [17, 6], INPOP [25, 4, 5] and 1 meter for INPOP and DE440.

Beside comparing LLRR coordinates obtained in different PA frames as in Table 2, one can also compare these coordinates with those obtained with other technics such as altimetry or imaging. In Sect. 2.2.4 are discussed results obtained in using LRO NAC images of the LLRR [12] and positions of LLRR obtained in the LRO Digitized Terrain Model derived by altimetry [16].

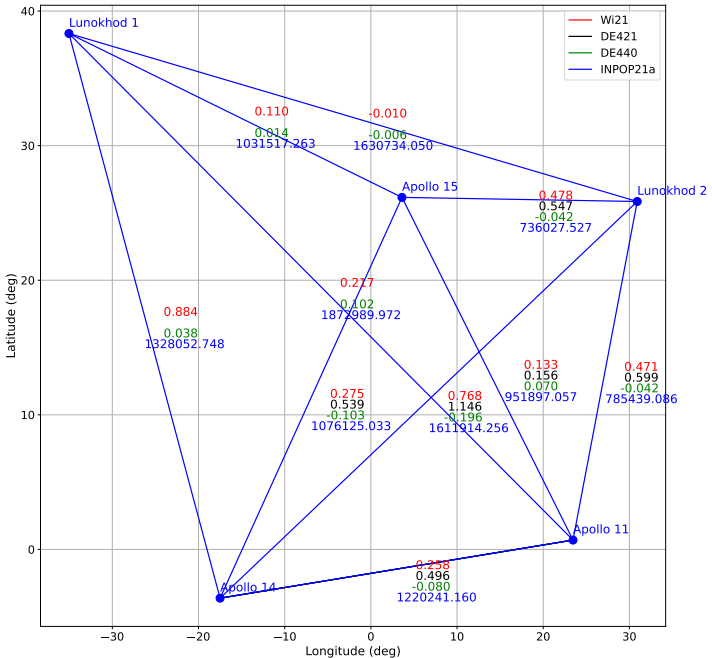


Fig. 3 Positions of the LLRR and differences in relative positions of LLRR for INPOP21a (blue value). The other colors represent the difference in relative positions with respect to the DE ephemerides and from [28].

2 Proposition of lunar reference systems: the LCRS and the LRS

2.1 The Moon-centered inertial Lunar Reference system, LCRS

Based on the concept of the GCRS as given in the IAU 2000 Resolution B1.3 [21, 19], we propose to define an inertial frame, labelled Lunar Celestial Reference System (LCRS), centered at the Moon center of mass, associated with a metric tensor based on [2] but adapted to the gravitational environment of the Moon. A lunar time scale is also defined associated with this metric tensor. This system will be used for the navigation and the integration of the equations of motion at the vicinity of the Moon.

2.1.1 Definition of the metric

By analogy with the definition of the GCRS metric tensor and the IAU 2000 Resolution B1.3 [21, 19], we consider the selenocentric metric tensor S_{ab} with selenocentric coordinates (T, \mathbf{X}) with T the Lunar Coordinate Time (TCL) and \mathbf{X} , the coordinate

vector of an orbiter in the LCRS. In the same manner, in the BCRS, we note t and \mathbf{x} , respectively the barycentric time-scale (TCB or TDB) and the coordinate vector of an orbiter. The selenocentric tensor is in the same form as the barycentric or the geocentric one but with Moon-centered potentials $L(T, \mathbf{X})$ and $L^a(T, \mathbf{X})$ such as:

$$S_{00} = -1 + \frac{2L}{c^2} - \frac{2L^2}{c^4}, S_{0a} = -\frac{4}{c^3} L^a, S_{ab} = \delta_{ab} \left(1 + \frac{2L}{c^2} \right). \quad (5)$$

The potentials L and L^a should be split into two parts - potentials L_S and L_S^a arising from the gravitational action of the Moon and external parts L_{ext} and L_{ext}^a due to tidal and inertial effects; the external parts of the metric potentials are assumed to vanish at the selenocenter and admit an expansion into positive powers of \mathbf{X}_L . Explicitly, one has

$$\mathbf{L} = L_S + L_{\text{ext}} + \mathcal{O}(c^{-4}) \quad (6)$$

$$\mathbf{L}^a = L_S^a + L_{\text{ext}}^a = -\frac{G}{2X^3} [\mathbf{X} \times \mathbf{A}_M] + \mathcal{O}(c^{-2}) \quad (7)$$

where \mathbf{A}_M is the Moon angular momentum. L_S correspond to the Newtonian Moon gravitational potential and L_{ext} is the tidal contribution produced by all the solar system bodies (excluding the Moon) estimated at the center of mass of the Moon (origin of the LCRS) and at $T=TCL$.

For the kinematically non-rotating LCRS, the transformation between BCRS and LCRS is given explicitly in using $T=TCL$, $t = TCB$, $\mathbf{r}_M = \mathbf{x} - \mathbf{x}_M$, the differences between the vectors of the BCRS barycentric position of the orbiter \mathbf{x} and the barycentric position of the Moon \mathbf{x}_M , \mathbf{v}_M and \mathbf{a}_M being the vectors of its barycentric velocity and acceleration. The dot stands for the derivative relative to t . The expression of the LCRS coordinate vector \mathbf{X} regarding the BCRS \mathbf{x} coordinate vector is given by

$$\begin{aligned} X = \mathbf{r}_M + \frac{1}{c^2} \left[\frac{1}{2} \mathbf{v}_M \cdot (\mathbf{v}_M \cdot \mathbf{r}_M) + l_{\text{ext}}(\mathbf{x}_M) \cdot \mathbf{r}_M + \right. \\ \left. \mathbf{r}_M \cdot (\mathbf{a}_M \cdot \mathbf{r}_M) - \frac{1}{2} \mathbf{a}_M \cdot r_M^2 \right] + \mathcal{O}(c^{-4}), \end{aligned} \quad (8)$$

with $l_{\text{ext}}(\mathbf{x}_M) = \sum_{A \neq M} \frac{GM_A}{r_{AM}} + \mathcal{O}(c^{-2})$ with $\mathbf{r}_{AM} = \mathbf{x}_A - \mathbf{x}_M$, the moon-centered vector of the body A in the BCRS.

The time transformation between BCRS time t and LCRS time T is

$$\begin{aligned} T_L = t - \frac{1}{c^2} \left[A(t) + v_M^i r_M^i \right] + \frac{1}{c^4} \times \\ \left[B(t) + B^i(t) r_M^i + B^{ij}(t) r_M^j r_M^i + C(t, \mathbf{x}) \right] + \mathcal{O}(c^{-5}), \end{aligned} \quad (9)$$

where v_M^i , r_M^i and a_M^i are the coordinates of the vectors \mathbf{v}_M , \mathbf{r}_M and \mathbf{a}_M respectively and

$$\frac{dA(t)}{dt} = \frac{1}{2} v_M^2 + l_{\text{ext}}(\mathbf{x}_M) \quad (10)$$

$$\frac{dB(t)}{dt} = -\frac{1}{8} v_M^4 - \frac{3}{2} v_M^2 l_{\text{ext}}(\mathbf{x}_M) + 4 v_M^i l_{\text{ext}}^i(\mathbf{x}_M) + \frac{1}{2} l_{\text{ext}}^2(\mathbf{x}_M), \quad (11)$$

$$B^i(t) = -\frac{1}{2} v_M^2 v_M^i - 3 v_M^i l_{\text{ext}}(\mathbf{x}_M) + 4 l_{\text{ext}}^i(\mathbf{x}_M), \quad (12)$$

$$B^{ij}(t) = -v_M^i \delta_{aj} Q^a + 2 \frac{\partial l_{\text{ext}}^i}{\partial x^j}(\mathbf{x}_M) - v_M^i \frac{\partial}{\partial x^j} l_{\text{ext}}(\mathbf{x}_M) + \frac{1}{2} \delta^{ij} l_{\text{ext}}(\mathbf{x}_M), \quad (13)$$

$$C(t, \mathbf{x}) = -\frac{1}{10} r_M^2 (\dot{a}_M^i r_M^i), \quad (14)$$

$$Q^a = \delta_{ai} \left[\frac{\partial}{\partial x^i} l_{\text{ext}}(\mathbf{x}_M) - a_M^i \right] \quad (15)$$

The expression of the potentials L_{ext} , L_S and L^a can be found for example in [23].

2.1.2 Definition of the Lunar Time-scale

The UTC time scale is used for the recording of the observations from the ground. For the definition of the selenodetic frames or when one uses the Earth-based observations for studying the dynamics of the moon, the UTC time scale is transformed into TDB [3].

The GPS Time (GPST) can be used as an intermediate time-scale between lunar orbiters and ground-based stations as it is proposed in the case of receivers of Earth GNSS signals in lunar orbit.

For the Moon surface datation or for the constellation orbiting the Moon, we define TCL, the relativistic time scale at the center of mass of the Moon, similar to the TCG, the relativistic time scale at the geocenter [21, 19]. Based on the previous equations, we can defined TCL as related to TCB such as TCG is related to TCB following [2] with:

$$\frac{dTCL}{dTCB} = 1 + \frac{1}{c^2} \alpha_L + \frac{1}{c^4} \beta_L + \mathcal{O}(c^{-5}) \quad (16)$$

with

$$\alpha_L = -\frac{1}{2} v_L^2 - \sum_{A \neq L} \frac{GM_A}{r_{LA}} \quad (17)$$

and

$$\beta_L = -\frac{1}{8} v_L^4 + \frac{1}{2} \left[\sum_{A \neq L} \frac{\mu_A}{r_{AL}} \right]^2 + \sum_{A \neq L} \frac{\mu_A}{r_{AL}} \left\{ 4 \mathbf{v}_L \cdot \mathbf{v}_A - \frac{3}{2} v_L^2 - 2 v_A^2 \right. \\ \left. + \frac{1}{2} \mathbf{a}_A \cdot \mathbf{r}_{AL} + \frac{1}{2} \left(\frac{\mathbf{v}_A \cdot \mathbf{r}_{AL}}{r_{AL}} \right)^2 + \sum_{B \neq A} \frac{\mu_B}{r_{BA}} \right\}, \quad (18)$$

Subscripts A and B enumerate massive bodies, L corresponds to the Moon, M_A is the mass of body A, $\mathbf{r}_{LA} = \mathbf{x}_L - \mathbf{x}_A$ (vectorial differences), r_{LA} is the norm of the vector \mathbf{r}_{LA} , \mathbf{x}_A is the barycentric vector of position of the massive body A, \mathbf{v}_A and \mathbf{a}_A are the barycentric vectors of velocity and acceleration of the massive body A with respect to TCB. α_L is of about 1.48×10^{-8} [23], and as explained in [15] and [23], the term β_L Eq. (18) is negligible for the present applications.

In the same way as TCL can be defined relative to TCB Eq. (16), it is also possible to describe TCL relative to TCG in the GCRS. In this case, we have

$$\frac{d \text{TCL}}{d \text{TCG}} = 1 + \frac{1}{c^2} \alpha_{L/G} + \frac{1}{c^4} \beta_{L/G} + \mathcal{O}(c^{-5}) \quad (19)$$

where $\alpha_{L/G}$ and $\beta_{L/G}$ have the same definitions as in Eqs. (17) and (18) but with geocentric positions and velocities.

$$\alpha_{L/G} = -\frac{1}{2} v_{L/G}^2 - \left[\sum_{A \neq L} \frac{GM_A}{r_{LA}} - \sum_{A \neq G} \frac{GM_A}{r_{GA}} \right] \quad (20)$$

In the other hand, TT is defined relative to TCG in such a way that [19]

$$\frac{d \text{TT}}{d \text{TCG}} = 1 - L_G \quad (21)$$

with $L_G = 6.969290134 \times 10^{-10}$. By considering that $\text{TCL-TT} = (\text{TCL-TCG}) + (\text{TCG-TT})$, with Eq. (16) and the current definition of TT Eq. (21), it can be deduced that

$$\frac{d \text{TCL-TT}}{d \text{TT}} = \frac{1}{1 - L_G} \times [L_G + \frac{1}{c^2} \alpha_{L/C} + \frac{1}{c^4} \beta_{L/C}] + \mathcal{O}(c^{-5}) \quad (22)$$

In Sect. 2.2.5, are given the results of the integration of Eq. (22) in the frame of the INPOP planetary ephemerides.

2.1.3 Transformation between BCRS and LCRS

From Eqs. (8) and (9) and explicit expressions of non-rotating potentials L and L_a , the transformation between the local lunar-centered reference frame coordinates of an object in the vicinity of the Moon, $\mathbf{X}(\text{TCL})$, also noted \mathbf{X} , and the coordinates of the same object in the BCRS relative to the Moon, $\mathbf{r}_M(\text{TDB})$, also noted r_M as in Eq. 8, is [21, 23]

$$\mathbf{r}_M = \mathbf{X} + c^{-2} \left[-\frac{1}{2} \mathbf{v}_M (\mathbf{v}_M \cdot \mathbf{X}) - \mathbf{X} \cdot l_{ext} + (\mathbf{w}_p \times \mathbf{X}) + \frac{1}{2} \mathbf{a}_M \cdot X^2 - \mathbf{X} (\mathbf{X} \cdot \mathbf{a}_M) \right] + \mathcal{O}(c^{-4}) \quad (23)$$

with \mathbf{w}_p being the vector associated with the relativistic precession (see i.e. [23]), \mathbf{v}_M and \mathbf{a}_M respectively the barycentric velocity and acceleration vectors of the Moon

(same notations as in Sect. 2.1.1), estimated at TDB. For the present day application in orbiter dynamics, the Eq. (23) can be simplified to [23]

$$\mathbf{r}_M = \mathbf{X}[1 - c^{-2} \sum_{b \neq M} l_b(\mathbf{r}_M^b)] - \frac{1}{2c^2} (\mathbf{v}_M \cdot \mathbf{X}) \mathbf{v}_M, \quad (24)$$

with $\sum_{b \neq M} l_b(\mathbf{r}_M^b)$ is the gravitational potential due to the solar system bodies except the Moon, at the Moon center of mass in the BCRS. For the velocity, with \mathbf{v} is the barycentric velocity of the orbiter in the BCRS at TDB, \mathbf{V} , its velocity in the LCRS at TCL, then the transformation for the velocities between BCRS and LCRS is given by [23]

$$\mathbf{v} - \mathbf{v}_M = [\mathbf{V}(1 - c^{-2} \sum_{b \neq M} l_b) - \frac{1}{2c^2} (\mathbf{v}_M \cdot \mathbf{V}) \mathbf{v}_M] \times \frac{dt_{TCL}}{dt_{TDB}}, \quad (25)$$

with $\frac{dt_{TCL}}{dt_{TDB}}$ deduced from by Eq. (16).

2.1.4 Accuracy assessments of the realization

The realization of the LCRS can be done using different lunar and planetary ephemerides. We consider here two generations of ephemerides, DE421 [27] which is the present reference for the definition of lunar ME frame (see Sect 1.4) and INPOP19a [4]. These two ephemerides differ as DE421 model does not account for the core-mantle interactions, the shape of the fluid core. More than 11 years of additional observations was also included in the INPOP19a construction. On Fig. 4 are plotted the differences in term of localization of the Moon relative to the Earth using DE421 and INPOP19a over 5 years. The maximum differences of about 1.5 meters are obtained in the Z direction. The ratio between the gravitational mass of the Earth-Moon barycenter obtained with DE421 and with INPOP19a differ from unity by $(1.2 \pm 10^{-11}) \times 10^{-8}$.

2.2 The lunar body-fixed reference system, LRS

In parallel to the LCRS, it is requested to define a frame attached to the Moon, as the ITRS has been defined as an Earth-attached frame. This frame, called LRS, will be defined based on the PA properties given in Sect 1.3 The realization of such a system could be obtained by using planetary and lunar ephemerides. In the next sections, we consider different accuracy assessments for the LRS realisations. We first consider the differences between the PA realisations using different planetary and lunar ephemerides (Sect. 2.2.1). We then consider the propagation of the PA covariance matrices with time (Sect. 2.2.2). We then discuss the link accuracy with other techniques such as altimetry and images obtained with LRO presented in Sect 2.2.4. Finally we consider derived time-scales that can be more appropriate than the TCL for the user localization or spacecraft navigation based on the definition proposed in Sect. 2.1.2.

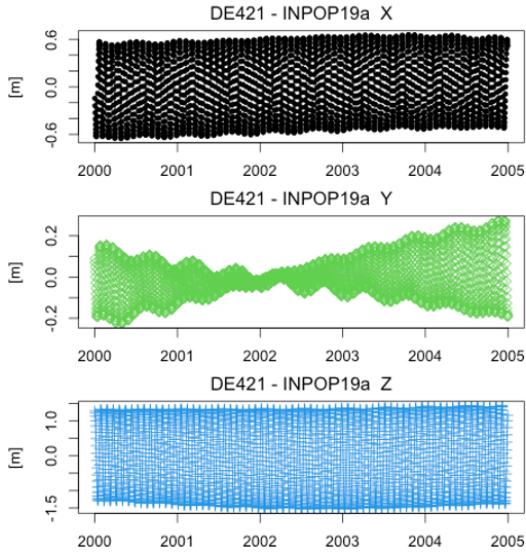


Fig. 4 Differences in meters on the Moon center positions relative to the Earth estimated with DE421 and INPOP19a in the ICRS.

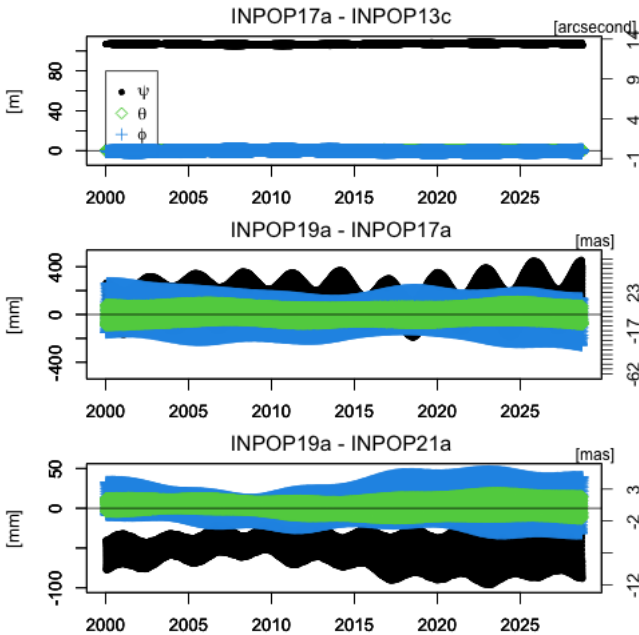


Fig. 5 Comparisons between the three libration angles of the Moon obtained with different ephemerides. The plotted differences are given in terms of displacement on the Moon surface (left-hand side y-axis) and in milli-seconds of arcs (right-hand side y-axis).

Table 3 Maximum Differences in libration angles (converted in meters on the Moon surface) between different generations of ephemerides over 30 years. Are also indicated the main differences in the dynamical model and data span between the compared eph

2000-2030	I17a-I13c	I19a-I17a	I19a-I21a	I19a-DE421
Differences in the model and in the data span	CMB interaction + 4 yrs LLR	Core shape + 2 yrs LLR	+2 yrs LLR	CMB interaction, core shape +11 yrs LLR
$\Delta\phi$	3 m	40 cm	6 cm	3 m
$\Delta\theta$	1.5 m	15 cm	3 cm	50 cm
$\Delta\psi$	3 m	50 cm	10 cm	1.6 cm
Offset in ψ	100 m		5 cm	

2.2.1 Comparisons between ephemerides

At present, the precision and accuracy of LRS realisations are limited by data accumulation, physical modelling and numerical fit. The Figure 5 shows the differences of rotational angles for various solutions of INPOP. The difference INPOP17a-INPOP13c (black, case I) represents the improvement in core-mantle interaction and accumulation of 4 years observations. The difference INPOP19a-INPOP17a (case II) is related to core-mantle oblateness and 2 years observations and finally INPOP19a-INPOP21a (case III) is 2 years observations. The improvement in the physical modeling (case I and II) reaches differences in the order of 3 meters (with 100 meters offset for ψ) and 50 centimeters respectively, meaning that there is still some possibility to improve the solution at the 50 cm level. The next step for physical modelling is (not in order of effect): solid core displacement, tidal deformation of the surface, visco-elastic contribution in deformation coefficients, impact of Earth Orientation Parameters. The accumulation of data (purely in case III) improves the solution by 10 cm over 2 years. The principal impact of observing longer would be to remove some bias introduced in the reduction analysis, while the principal impact of adding new reflectors on the Moon surface will be to better disentangle the different contributions of the libration mis-modeling and to help for a better study of physical unknowns described previously.

In conclusion, with the most up-to-date modeling, the differences in the libration angles should not exceed 30 to 50 cm over 5 years. On Table 3, we give a summary of the previous comparisons between INPOP solutions but also are indicated the maximum differences in libration angles between INPOP19a and DE421 over the 30 year period.

The main characteristics of INPOP21a can be found in Table 4.

2.2.2 Propagation of the covariance matrix

An other possible way to assess the accuracy of the LRS realisations is also to consider its stability according to time. This can be done by propagating the covariance matrix of the libration angles with time following the method proposed by [22]. If $H(t_0)$ is the covariance matrix of the lunar libration angles (ψ , θ , φ) at the reference time of the ephemeris t_0 (for INPOP, t_0 is J2000) we can then study the evolution of the uncertainties $H(t)$ for these angles at any date t by considering the Jacobian matrix $J(t)$ and with $H(t) = J(t) H(t_0) J^T(t)$. For this analysis, we use the covariance matrix and the partial derivatives of INPOP21a.

Table 4 Table of interoperability and application to INPOP21a.

	Parameters/models to be fixed by convention	INPOP21a
LLR data analysis		
LLR data sample	by convention with open access	[5], Table 4 and Figure 10
station positions		Table 7 in [5]
IRTF to ICRF	IERS convention	[19] section 5
outlier filtering		[6] section 5.1.2
bias	in principle by convention	[24] section 5.1.2
Dynamical model		
Earth tides and gravity field	IERS convention 2010	[25] section 2.2.1 [24] section 3
Moon tides and gravity field		[25] section 2.2.1 [24] section 3
Rotational equations		[25], Eqs 1 and 2a-2e
Translational equations		[25] section 2.2.1
Internal structure interactions		[25], Eqs 1 and 2a-2e
adjustement weight		[26], Eqs 1-3 and appendix A
method of adjustment	Least squares	[24] section 5.1.2 [25] section 2.4
LRF definition and delivery		
Definition of the ME frame	Eqs in Sec 1.4	
Definition of the PA frame	Euler angles Eq. 1	
Definition of time-scales	Eq. 22 in Sec. 2.1.2	
Delivery of PA frame	Chebyshev polynomials with fixed orders	for TT-TDB see Eq. In [3] , Eqs 7 to 10 calceph
Delivery of time-scales	depending the precision required	TT-TCL not implemented yet TT-TDB chebyshev polynomials based on calceph

With the initial uncertainties for (ψ, θ, φ) of about (6.0, 0.1, 0.3) milli-seconds of arcs (mas) respectively, the result of the propagation of the covariance is given in Figure 6. The maximum is obtained for ψ with 35 cm over 25 years. This is stable and consistent with the comparisons of the recent INPOP versions, INPOP17a, INPOP19a and INPOP21a.

2.2.3 Impact of reference frame on gravity field and orbit computations

As it has been explained in Sect. 1.4, the estimations of gravity field from radio-science experiments on board of Moon exploration missions such as GRAIL or LRO have been considering a specific PA frame obtained from the DE421 planetary and lunar ephemerides [11]. In the perspective of using different PA frames, it is then important to consider the impact of changing the reference frame in i) the estimation of gravity field coefficients and ii) in the computation of s/c orbit.

Gravity field

In order to estimate the impact of such a transformation, we first consider the transformation from the GRAIL GL0420A [11] gravity field coefficients from DE421 PA

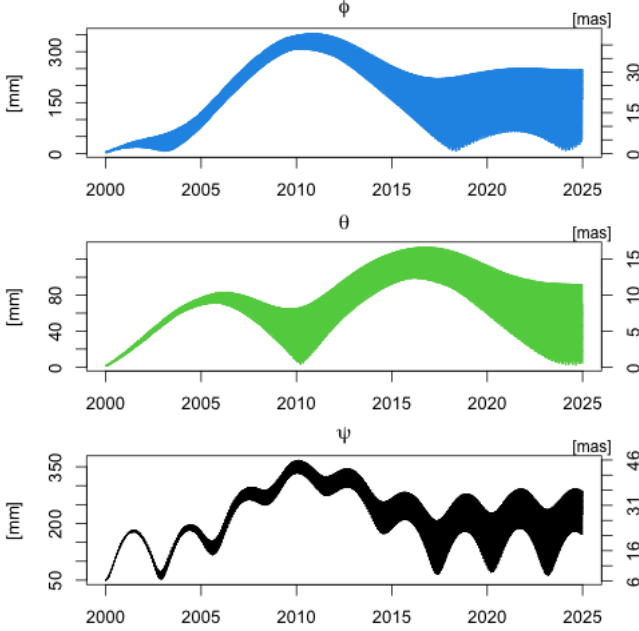


Fig. 6 Propagation of the INPOP21a covariance matrix for the three libration angles (ψ , θ , φ). The results are given in terms of displacement on the Moon surface (left-hand side y-axis) and in milli-seconds of arcs (right-hand side y-axis).

frame to LCRF by applying the relation

$$GF_{LCRF} = R_z(-\psi_{DE421}) R_x(-\theta_{DE421}) R_z(-\varphi_{DE421}) GF_{DE421} \quad (26)$$

where $(\psi_{DE421}, \theta_{DE421}, \varphi_{DE421})$ are the libration angles defining the DE421 PA frame. Following [7], we also account for the translation from the center of mass of DE421 to the center of mass of INPOP19a at the reference epoch of GL0420A (see Fig. 4) and the scaling factor between the Moon mass of DE421 and the one of INPOP19a. The ratio between the mass of the Moon in DE421 and the mass of the Moon in INPOP19a is $1 + 1.2 \times 10^{-8}$. We then transform the GF_{LCRF} to the $GF_{INPOP19a}$ in using the following relation

$$GF_{INPOP19a} = R_z(\varphi_{INPOP19a}) R_x(\theta_{INPOP19a}) R_z(\psi_{INPOP19a}) GF_{LCRF} \quad (27)$$

with $(\psi_{INPOP19a}, \theta_{INPOP19a}, \varphi_{INPOP19a})$ are the libration angles defining the INPOP19a PA frame.

We note $d_C = C_{DE421} - C_{INPOP19a}$ (respectively d_S), the differences in C (respectively S) coefficients in DE421 PA (C_{DE421}) and C (respectively S) coefficients in INPOP19a PA ($C_{INPOP19a}$). We then define

$$\delta C = \frac{d_C}{\sigma_C} \text{ and } \Delta C = \frac{d_C}{C_{DE421}} \quad (28)$$

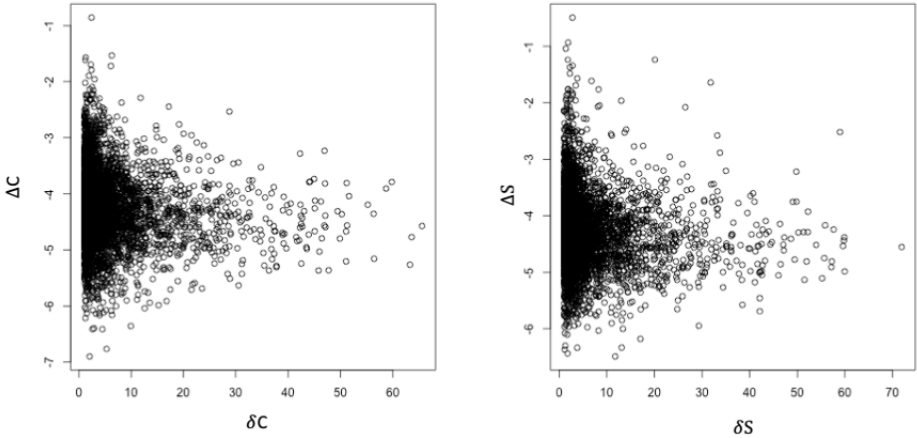


Fig. 7 Differences between DE421 PA and INPOP19a PA C (on the left) and S (on the right) coefficients over 5 years. The gravity field coefficients are those from GRAIL GL0420A [11]. On the x-axis are plotted the ratio between the C and S differences and GRAIL GL0420A uncertainties. On the y-axis, are plotted the log of the ratio of the differences and DE421 C (or S) coefficients as provided by GL0420A.

where σ_C the GRAIL GL0420A uncertainty on the C coefficients (σ_S for S coefficients, respectively). On Figure 7 are plotted ΔC versus δC .

The differences were plotted over 5 years. On these plots one can see that the coefficients with differences significantly greater than the uncertainties are those for which the amplitudes are the smallest. In particular, the coefficients have a ratio differences versus uncertainties greater than 10 are those for which the ratio differences versus amplitudes are smaller than 0.01.

s/c orbit computation

Differences between lunar reference frames defined on different planetary ephemerides can be organised as follow

- Differences in the dynamical scale – the product of the gravity constant and lunar mass. In the case of the DE421 and INPOP19a differences, this difference is of about 1.2×10^{-8}
- Differences in the geometrical scale – the radius of the Moon,
- Differences in the orientation of the reference frame – rotation of the selenoid.

On the International Centre for Global Earth Models (ICGEM) one can find different lunar gravity field models obtained since 1994. Despite that the latest models are based on GRAIL data, some obvious differences between the models occur. For example, the gravitational mass of the Moon value varies of about $5 \times 10^{-3}\%$ to $2 \times 10^{-3}\%$ between GrazLGM420b, GRGM660PRIM and AIUB-GRL350A. Changing the gravitational mass of the Moon directly impacts the satellite revolution period and satellite radial orbit component. Furthermore, the degree-1 parameters of the lunar gravity field define the origin of the reference frame (the center of mass). For the gravity field models coinciding with the center-of-mass of a celestial body, the degree-1 coefficients should be nullified.

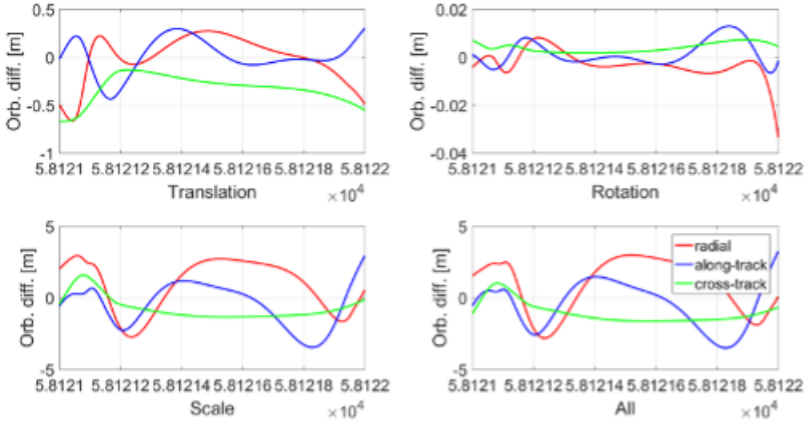


Fig. 8 Differences between DE421 and INPOP19a due to translation, rotation, scale difference, and all transformation parameters on the orbits derived in one reference frame (DE421) and reconstructed using selected parameters from the second reference frame (INPOP19a)

To assess the impact of the reference frame differences between DE421 and INPOP19a, the GRAIL gravity field has been re-scaled, rotated, and translated according to the transformation parameters between DE421 and INPOP19a described in Section 2.2.3. We analysed the impact of the reference frame differences on the orbit reconstruction, i.e., the reference orbit has been integrated in the DE421 reference frame and stored as a series of positions (X, Y, Z) every 30 seconds for 1 day. Next, we check the impact of replacing the reference parameters by considering from INPOP19a:

- the scale parameter,
- the translation parameters,
- the rotation parameters,
- the scale + translation + rotation parameters, i.e., the full transformation between DE421 and INPOP19a.

Figure 8 shows the differences in the reconstructed orbit of lunar orbiters due to the differences in translation, rotation, scale, and all transformation parameters between DE421 and INPOP19a. Differences between rotation parameters of a selenoid introduce a marginal effect of -2, 2, and 4 mm of the mean bias for the radial, along-track, and cross-track components, respectively. The RMS error due to the rotation does not exceed 5 mm, thus, can be neglected. However, the scale and origin must be consistent between reference frames. The mean translation error is equal to 4, 16, and -323 mm for the radial, along-track, and cross-track components, respectively with the RMS values of 238, 179, and 139 mm. The errors generated by the scale differences are at the meter level: 909, -463, and -707 mm for the mean bias and 1775, 1497, and 795 for the RMS of the radial, along-track, and cross-track components, respectively. Thus, we can conclude that the differences of the rotation cause differences at the mm-level, differences of the translation cause differences at

Table 5 Mean and RMS of differences (in meters) for the three components (Radial, Along-Track and Cross-Track) of the orbits integrated in INPOP19a reference frame w.r.t. DE421 without and with adjusting a posteriori Helmert transformation parameters

	Radial m	Along-Track m	Cross-track m
Without Helmert	0.908 ± 1.846	-0.447 ± 1.607	-1.028 ± 0.727
With Helmert	-0.102 ± 1.748	0.070 ± 1.484	0.00 ± 0.238

the dm-level, whereas differences of the scale cause differences at the m-level for the reconstructed orbits. Therefore, the translation and scale parameters have to be treated consistently, whereas the rotation of the selenoid plays a minor role on the reconstructed orbits. The differences between reference frames can be mitigated, to a certain extent, by estimating 7-Helmert transformation parameters that account for the rotation, scale, and origin offset. Table 5 shows the mean offsets and RMS of the radial, along-track, and cross-track orbit components without and with estimating a posteriori Helmert parameters. The estimated Helmert parameters reduce the mean orbit offsets in the along-track and cross-track components. However large errors remain for the radial (which is sensitive to the dynamical scale difference) and RMS values of all components, because the orbit is integrated and not just geometrically translated, rotated, and re-scaled. Large errors still remain after estimating the Helmert parameters for the integrated orbits; Thus, the consistency in a priori reference frames is indispensable as it cannot be accounted for in the a posteriori transformation.

Finally, we verified the differences between DE421 and INPOP19a for the orbit extrapolation. We took the state vector (position + velocity) for one epoch determined in DE421 and extrapolated the orbit using the numerical integration in the INPOP19a reference frame. This test shows the differences between reference frames in terms of scale, origin, and orientation. Figure 9 shows the impact of the reference frame differences on the orbit extrapolation. After 1-day, the differences exceed 20 and 45 m for the radial and along-track components, respectively. Moreover, as opposed to the orbit reconstruction based on the position series, no RMS values can be estimated when having only the initial state vector, thus, the possible error due to the reference frame differences cannot be identified. Therefore, for the orbit predictions, the reference frame must be treated consistently. Information on the satellite state vector must always be accompanied by the information on the reference frame and force models that were the foundation for deriving its value. Otherwise, the errors may reach tens of meters after just one hour of the orbit integration.

2.2.4 Link to LRO DTM

As it has been discussed in Sect. 1.6, assessments about the definition of the lunar frame can be done by considering the uncertainties of the rotation modelling (see Sect. 2.2.1 and 2.2.2) but it can also be addressed considering the question of how to link the lunar reference frame defined in Sect. 1.6 to the Digital Terrain Model (DTM) obtained with images and altimetric data from space missions such as Lunar Reconnaissance Orbiter (LRO). In 2018, a first tie between LRO DTM and ME DE421 has been obtained by [16] and an other independent tie has been realised with LRO

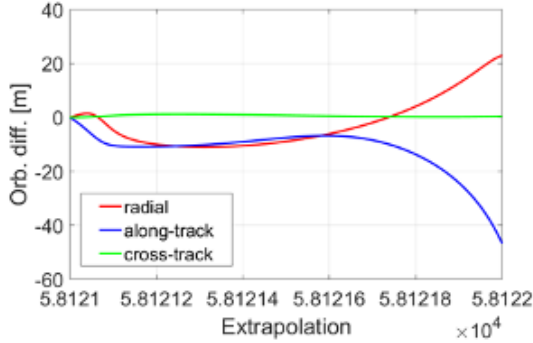


Fig. 9 Differences between DE421 and INPOP19a on the extrapolated orbit derived as a state vector in one reference frame (DE421) and extrapolated in the second reference frame (INPOP19a)

NAC camera [12]. With [12], comparisons between positions of the LLRR observed by LRO NAC cameras and LOLA altimetric data and positions deduced from JPL DE421 were done and give maximum differences of about 10 meters, comparable to the RMS of LRO orbit overlaps [14]. We have shown in Sect. 1.6 that the differences between LLRR positions deduced from different lunar ephemerides are of about 1 meter (see Table 2). So, we can infer that the present link to LRO DTM accuracy is limited by the LRO orbit overlap accuracy, to 10 meters.

2.2.5 LRS Time-scales

The time-scales associated with LRS could be a realisation of TCL defined in Sect. 2.1.2, but other time-scales can also be proposed depending the requested location of the datation (at the Moon center, at the Moon surface, on board the orbiter). The Eq. (22) could be integrated independently from the planetary and lunar ephemeris chosen for the LCRS and LRS realisation using a simple integrator or directly with the planetary ephemerides. After a simultaneous integration with planetary orbits, TCL-TT is given in Figure 10. It appears that TCL-TT can be decomposed in two parts: a secular drift of about $58.7\mu\text{s}$ per day and a periodic term with an amplitude of about $0.6\mu\text{s}$ and a period of 27.8 days. These two terms match with the expected trend that one could obtain by the addition to L_G of the term accounting for the gravitational potential of the Earth on the Moon, approximated by $-\frac{3}{2c^2}\frac{GM_E}{a_M}$, with a_M being the semi-major axis of the geocentric Moon orbit and GM_E , the gravitational mass of the Earth. The periodic term is compatible with the effect of the Moon eccentric orbit and can be approximated with $\frac{2}{c^2}\sqrt{GM_E a_M} e_M \sin E_M$ with e_M and E_M being respectively the eccentricity and the eccentric anomaly of the Moon orbit. The differences between the full integration and the approximated terms ($L_G - \frac{3}{2c^2}\frac{GM_E}{a_M} - \frac{2}{c^2}\sqrt{GM_E a_M} e_M \sin E_M$) will be of about $0.2\mu\text{s}$.

The right side of Figure 10 shows an additional low frequency component with a period around ~ 6 months. These other harmonics are induced by the non-Keplerian motion of the Moon relative to the Earth. The orbit of the Moon about the Earth is indeed computed with the full model of perturbations including Sun, planetary

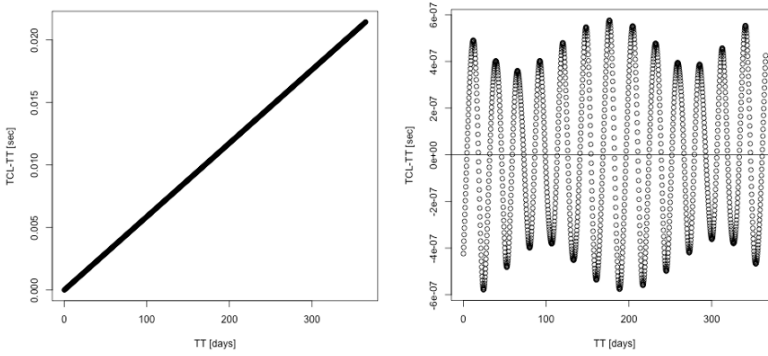


Fig. 10 On the left-hand side, (TCL-TT) versus Time in TT (days). On the right-hand side, (TCL-TT) versus Time in TT (days): the remaining periodic term after the drift removal of about $58.7 \mu\text{s}$ per day in (TCL-TT). For the two plots, the results are given in s

contributions, tides etc... So, it is normal that other harmonics are present even if we integrate here only the contribution of the Earth potential on the Moon (perturbed in the full formalism) for the computation of TCL.

For a datation at the Moon surface, it is necessary to account for the difference of potential between the time at the selenocenter (TCL) and the time at the surface (TCLS). TCLS can be obtained for a clock at the Moon surface with R_c and V_c its position and velocity relative to the selenocenter at time t and t_0 , such as:

$$TCL - TCLS = \frac{1}{c^2} \frac{GM_M}{R_M} \Delta t + \frac{1}{c^2} (R_c(t) \cdot V_c(t) - R_c(t_0) \cdot V_c(t_0)) \quad (29)$$

For a clock at rest on the surface, the second term is 0. The corresponding TCLS is noted $TCLS^*$ in the following. The first term of the previous equation induces an additional secular drift of about $2.7 \mu\text{s}$ per day (3.141×10^{-11}) for a fixed clock on the Moon surface. Finally for a Moon orbiter, depending its orbit, the time on board (TCLO) can be deduced from the $TCLS^*$, the time as indicated by a clock at rest on the surface, by

$$TCLS^* - TCLO = \frac{2}{c^2} \mathbf{R}_O \cdot \mathbf{V}_O + \left(\frac{3}{2c^2} \frac{GM_M}{a} - \frac{1}{c^2} \frac{GM_M}{R_M} \right) \times \Delta t \quad (30)$$

with R_O and V_O the position and velocity of the orbiter relative to the selenocenter. This difference can also be written in supposing that the orbit is elliptic with

$$TCLS^* - TCLO = \frac{2}{c^2} \sqrt{GM_M a} e \sin E + \frac{GM_M}{c^2} \left(\frac{3}{2a} - \frac{1}{R_M} \right) \times \Delta t \quad (31)$$

where a is the semi-major axis of the satellite orbit, e its eccentricity and E its eccentric anomaly.

For a circular orbit with a semi-major axis of 10 000 km and $e=0.01$, the effect on the time scale will be a periodical term with an amplitude of about 1.5 ns with a drift of $-2.24 \mu\text{s}$ per day (-2.59×10^{-11}) when for an eccentric orbit ($e=0.5$) with $a=5000$ km, the amplitude of the periodical effect will be of about 27 ns with a drift of $1.76 \mu\text{s}$ per day (-2.05×10^{-11}).

Based on these results, we propose to define a Lunar time scale TL defined such as

$$\frac{dT_L}{dT_{CL}} = (1 - L_L) \quad (32)$$

with $L_L = 6.796 \times 10^{-10}$. The differences between TL and TT will be then only the periodic part visible in Figure 10. A broadcast of this periodic term can be proposed as a convenient and easy way to distribute Lunar Time together with the Ephemeris. Finally, the correction of the time scale fluctuations induced by the eccentricity of the satellite orbit (mainly the terms of the TCLS-TCLO) must be estimated and taken into account in the user's receiver.

The previous results have been obtained in considering only the effect of the Earth on the Moon. If one adds the differential contributions of the Sun and the other planets on the Earth-Moon system, the previous linear trend is still valid, but the period term is modified by a quasi-annual term (1.13 yr) of an amplitude of about 15 μs . The final definition and realization of TCL is currently under discussion.

3 Simulations for future improvements

In this section, we present results of simulations assessing the level of improvement in the covariance matrix of the libration angles defining the PA frame (and consequently the LRS). We consider two scenarios: in the first one, we investigate the improvement brought by the installation of additional retro-reflectors on the Moon surface following [29]; in the second one, we estimate the improvement brought by altimetric observations obtained from MoonLight possible orbits.

3.1 Improvements with additional reflectors

Through this section, we explore the possibility of an improvement in the PA angles (see Section 1.3) covariance matrix by having additional reflectors (LRR) on the lunar surface. In addition to the availability of more LLR (Lunar Laser Ranging) observations, it also presents an opportunity to have lower uncertainties in the measurements themselves as both equipment at stations and analysis models will improve over time. The locations of the five existing and simulated retroreflectors are listed in Table 6.

LLR measurements can be estimated using a numerically integrated ephemeris. Several parameters influence accurate range measurements to LRRs [25]. These include:

- Initial conditions of the position and the velocity for the Moon (PV) with respect to the Earth in the ICRF2 reference frame, at the start of the integration time (JD 2451544.5 in TDB).

Table 6 Coordinates of five existing and simulated retroreflector sites. The stars indicate new tested locations for future possible LLRRs.

Site	Long (deg)	Lat (deg)	X (km)	Y (km)	Z (km)
Apollo 11	23	1	1592	691	21
Apollo 14	-17	-4	1653	-521	-110
Apollo 15	3	26	1555	98	765
Lunokhod 1	-35	38	1114	-781	1076
Lunokhod 2	31	26	1339	802	756
South Pole*	0	-88	61	0	-1736
North Pole*	0	88	61	0	1736

- Initial conditions of the Euler angles and the angular velocities for the full Moon (AL).
- Gravitational mass of the Earth-Moon barycenter (GM_{EMB}).
- Initial conditions of the angular velocities for the lunar fluid core with respect to the mantle frame.
- Polar moment of inertia of the Moon.
- Oblateness of the lunar fluid core which characterizes the difference between the equatorial and polar diameters of the fluid core.
- Coefficient of viscous friction at the core-mantle boundary due to the relative motion of the lunar mantle and the lunar fluid core at the lunar core-mantle boundary.
- Lunar tidal time delay.
- Gravity field coefficients of the Moon.
- Horizontal and vertical tidal lunar Love numbers ($h_{2,M}$, $l_{2,M}$)

The covariance matrix with these parameters depicts how each parameter varies with others and gives the accuracy of the model in comparison to the LLR observations. It is constructed using partial derivatives of each of these parameters, obtained by simulating ranges and modifying the ephemeris with appropriate delta (numerical differentiation).

In order to simulate range between ground stations and LLRRs, we use the ESA software GODOT. GODOT is the ESA/ESOC flight dynamics software for performing orbit-related computations for estimation, optimization, and analysis of orbits for mission analysis and in-flight operations (<https://godot.io.esa.int/docs/0.9.0/index.html>). It is intended as a generic, extensible system for use in practically any space mission. GODOT can simulate ranges to LLRRs from stations on Earth with appropriate ephemeris. In order to impose the monthly observational selection effects for the LLRR sites on the corresponding simulated ranges, we used existing OCA ground station observations for simulating ranges. Hence partial derivatives with respect to each parameter and covariance matrix are obtained following a realistic distribution of the data. This approach was proposed by [29].

Additional retroreflectors were simulated for times from the beginning of 2014 till the end of 2021 as per observations to Apollo sites that were publicly available (<http://polac.obspm.fr/llrdatae.html>). We used existing OCA ground station data for the Apollo 15 reflector for the times of the simulated observations to the South Pole or the North Pole in order to impose the monthly observational selection effects for the

Apollo sites on the corresponding simulated data. Since Apollo 15 reflector acquired a lot more ranges than the other sites, we only used the dates for every third observation [29]. Hence 1015 ranges were simulated between 2014 and 2021 to the new additional retroreflector sites at the South and North poles.

We need to have uncertainty estimates for the observations to the simulated LLRR. This is accomplished by making four assumptions for each South Pole and North Pole LLR observation [29]. According to Range Uncertainty Assumption Set 1 or RUAS1, the simulated range uncertainty is assumed to be the same as that from the OCA Apollo 15 observation. This is a conservative assumption where the ratio of the uncertainty of the simulated range to the uncertainty of OCA Apollo is 1 even when the new retroreflectors should do better than the older ones. Whereas in RUAS2, this ratio is 0.5 and is a realistic assumption with the existing station equipment and analysis model. In RUAS3, the ratio is 0.1, and equipment at the stations and the analysis model should be improved to achieve this. In RUAS4, the ratio is 0.01 and this requires advanced ranging equipment and advanced modeling, which will serve as a goal for future improvements.

The covariance matrix gets updated with the addition of simulated observations to the new retroreflectors with appropriate RUAS as discussed above. The uncertainty associated with a parameter, j is given as,

$$\sigma_j = \sqrt{\text{cov}(j, j)} \quad (33)$$

where cov are the covariance coefficients. The improvement in percentage, I_j in uncertainty of a parameter is calculated as,

$$I_j = \frac{\Delta\sigma_j}{\sigma_j} \times 100 \quad (34)$$

with $\Delta\sigma_j$, the difference between the uncertainty for parameter j before and after adding the new LLR observations. There will be 4 sets of covariance matrices as there are 4 range uncertainty assumption sets (RUAS). The greatest improvement in uncertainties happens for the tidal Love number corresponding to horizontal solid body tide, l_2 (80%), and the gravitational mass of the Earth-Moon barycenter, GM_{EMB} (72%) in the most conservative range uncertainty assumption or RUAS 1. Figure 11 depicts the improvement in positional vector and libration angles with all four range uncertainty assumption sets.

For the first RUAS, the improvement in positional vectors (PV) lies between 1% and 21% whereas the addition of retroreflectors causes only a 4% improvement for libration angles (AL). But as RUAS goes higher to RUAS 2, RUAS 3, and RUAS 4, the uncertainty of the simulated observations goes lower and the weight of these simulations goes higher in the process of calculating the covariance matrix. In the case of PV, by RUAS 4 there is improvement in the range of 55% to 90% whereas this value is between 44% and 56% for libration angles (AL). Patterns among components of PV (PV1, PV2, PV3, PV4, PV5, PV6) and AL (AL1, AL2, AL3, AL4, AL5, AL6) are similar because of high correlation, although not identical. Improvement in vertical tidal Love number h_2 , horizontal tidal Love number l_2 and

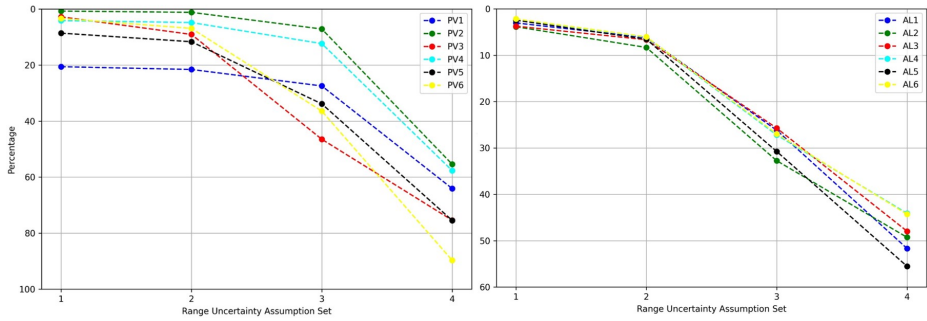


Fig. 11 Improvement in % for positional vector (PV on the left) and libration angles (AL on the right) with range uncertainty assumption sets.

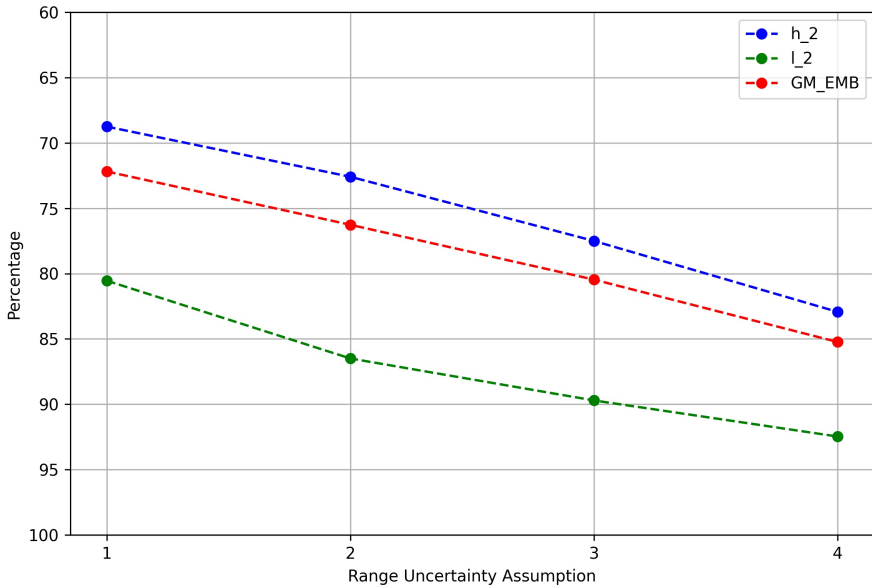


Fig. 12 Improvement in % for h_2 , l_2 and GM_{EMB} with range uncertainty assumption sets.

Gravitational mass of the Earth-Moon barycenter (GM_{EMB}) with range uncertainty assumption sets is shown in Figure 12.

In the overly conservative range uncertainty assumption (RUAS 1) gives an improvement of 69%, 81% and 72% respectively for h_2 , l_2 and GM_{EMB} . This goes up to 73%, 86%, and 76% for the more realistic RUAS2. It again goes higher to 78%, 90%, and 80% for RUAS 3 and 83%, 92%, and 85% for RUAS 4.

Adding new retroreflectors on the lunar surface always adds to the information available to significantly better define the Earth-Moon system and PA frame definition.

Table 7 Moon-centered spacecraft cartesian initial conditions given at 2026 June 01 00:00:00 TDB

	Positions km	Velocities km.s ⁻¹
<i>x</i>	-2181.20	-0.32
<i>y</i>	-9576.67	-1.29
<i>z</i>	2601.48	-0.72

3.2 Improvements with MoonLight altimetry

In addition to the proposed improvements in the definition of the Moon reference system by additional Lunar Laser Ranging retroreflectors (LLRRs), there is a possibility of employing a spacecraft revolving around the Moon equipped with an altimetric device in addition to LRR. The prospective spacecraft ($\sim 800'$) will carry out laser ranging with the proposed LLRR installed on the Moon's surface. Based on the present orbital configuration of the MoonLight constellation, it appears that the North Pole LLRR is in this case the most appropriate reflector to be tracked by the laser altimetry on board the spacecraft as it is closest to the currently proposed spacecraft orbit. The initial conditions (2026 June 01 00:00:00 TDB) for the spacecraft orbit from the center of the Moon in the J2000 frame are given in Table 7.

The scope of these simulations is not to discuss the feasibility of such measurements but to assess the gain for the definition of the PA frame if such altimetric campaign takes place with different range of possible accuracies.

This ranging experiment is carried out for a period of 1 year from the initialization period, i.e. until 2027 June 1 00:00:00 TDB.

The motion of the spacecraft is integrated using GODOT. It is constrained by several components including ephemeris, gravity, etc. During this period, we sampled or had ranges at 368 instances. These 368 ranges correspond to times when the proposed North Pole-spacecraft range is the shortest which also implies that the time taken by spacecraft for one revolution around Moon is close to 1 day. The position of the spacecraft from June 01, 2026 to June 30, 2026 is shown in Figure 13.

Once again, we use the ESA/ESOC flight dynamics software GODOT for integrating the orbit of the spacecraft and estimating the spacecraft-North Pole range. The integration of the spacecraft orbit is done in the ICRF centered on the Moon. Later the vectors to the spacecraft and the North Pole are resolved to compute the spacecraft-North Pole range using the procedure described in Sections 1.3 and 3.1. A simplification is done here in not applying the PA transformation also to the gravity field coefficients.

Since the spacecraft is operational from June 01, 2026 we extended the existing LLR observations from January 01, 2022 to December 31, 2027 for a period of 6 years with a statistical sampling similar to that from January 01, 2015 to December 31, 2020. As discussed earlier, one observation was simulated to North Pole LLRR for every 3 observations to Apollo 15 reflector and this accounted for 1864 observations between the beginning of 2014 and the end of 2027.

The covariance matrix is updated with the updated partial derivatives including the additional observations (to existing LLRRs and simulated LLRR at the North Pole) and ranges (between the LLRR at the North Pole and the spacecraft). This

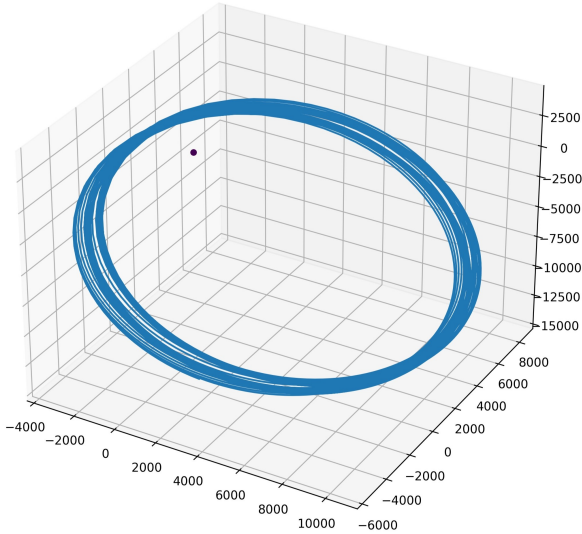


Fig. 13 Spacecraft position from June 01, 2026 to June 30, 2026, with the center of Moon at the origin. The violet dot represents the location of the simulated LLRR at the North Pole.

process involves having four assumptions for range uncertainty (RUAS 1, RUAS 2, RUAS 3 and RUAS 4) for the simulated North Pole LLRR as discussed in the section 3.1. In addition to this, it is necessary to have an uncertainty estimate for the range between North Pole LLRR and the spacecraft. Several simulations were carried out with different uncertainties from 10 m to 1 cm. Driven by our aim to improve uncertainty, it was found that noticeable improvement was found only when the range uncertainty is as low as 1 cm.

Not all the parameters have their accuracies improved by the use of altimetric measurements in addition to the North Pole LLRR. One Figure 14 and 15, are plotted for only parameters sensitive to MoonLight altimetry, the improvements in % induced by the use of North Pole LLRR in one hand (without s/c) and the use of North Pole LLRR and MoonLight altimetry (with s/c) in the other hand for for the 4 scenarii of LLR accuracies considered in Section 3.1 and in considering an accuracy of 1 cm for the MoonLight altimetry.

As one can see on Figure 14, the tidal Love number corresponding to horizontal solid body tide, l_2 benefits the most by the addition of the ranges from Earth to North Pole but it is h_2 that sees its accuracy improved the most by the addition of the ranges between spacecraft and the LLRR at the North Pole for all the RUAS. There is a 13 % improvement in the corresponding uncertainty with RUAS 1 and LLRR-spacecraft range uncertainty at 1 cm. For parameters like tidal Love number corresponding to horizontal solid body tide, l_2 and the gravitational mass of the Earth-Moon barycenter, GM_{EMB} the difference in improvement with and without s/c , is 4% and 10% respectively with RUAS 1. But for these two parameters, the improvement decreases significantly when the accuracies of the LRR increases for the RUAS 2, RUAS 3

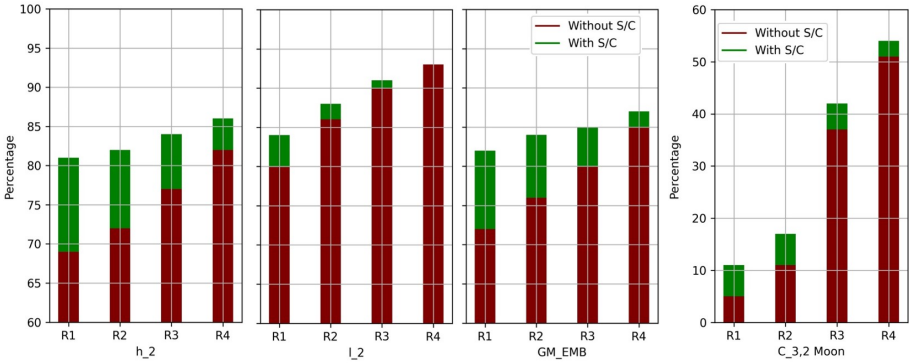


Fig. 14 Improvement in % for h_2 , l_2 , GM_{EMB} and C_{32} on the addition of spacecraft with 1-cm accurate range measurement between the s/c and the North Pole LLRR, along with the LLRR range uncertainty assumption sets.

and RAUS 4. By improving significantly the accuracy of the LLR, most of the information on l_2 and the gravitational mass of the Earth-Moon barycenter, GM_{EMB} is brought by LLR and the addition of the s/c ranges with an accuracy of 1 cm does not help for improving their determinations.

Similarly, the improvement in the uncertainty of libration angles with spacecraft in multiple spacecraft-LLRR range uncertainty scenarii is shown in figure 15. AL1, AL3 and AL5 see a good sensitivity to s/c ranges whatever is the RAUS. For AL2, AL4 and AL6, the information brought by MoonLight altimetry is marginal for all RAUS. Finally one can notice the sensitivity of the degree 3 order 2 C coefficient of the Moon gravity field which also seems to gain in accuracy thanks to the MoonLight 1-cm altimetry.

In conclusion, the addition of ranges from LLRR-spacecraft in the MoonLight constellation is indeed improving the uncertainty estimate for some parameters (mainly the Love numbers, the GM_{EMB} and the C_{32}) in a scenario where the range between the s/c and the North Pole reflector can be done with at least a 1-cm accuracy. The impact on the PA angles is marginal but non negligible. The size of the improvement may also be dependent on several parameters especially the uncertainty in the LLRR-spacecraft range (RUAS) as discussed earlier.

Acknowledgements

The authors wish to thank the participants of the ATLAS consortium, to ESA members P. Giordano, R. Swinden and J. Ventura-Traveset as well as J. Laskar and M. Gastineau for the development of the INPOP planetary ephemerides

References

[1] Archinal BA, Acton CH, A’Hearn MF, Conrad A, Consolmagno GJ, Duxbury T, Hestroffer D, Hilton JL, Kirk RL, Klioner SA, McCarthy D, Meech K, Oberst J, Ping J, Seidelmann PK, Tholen DJ, Thomas PC, Williams IP (2018) Report of

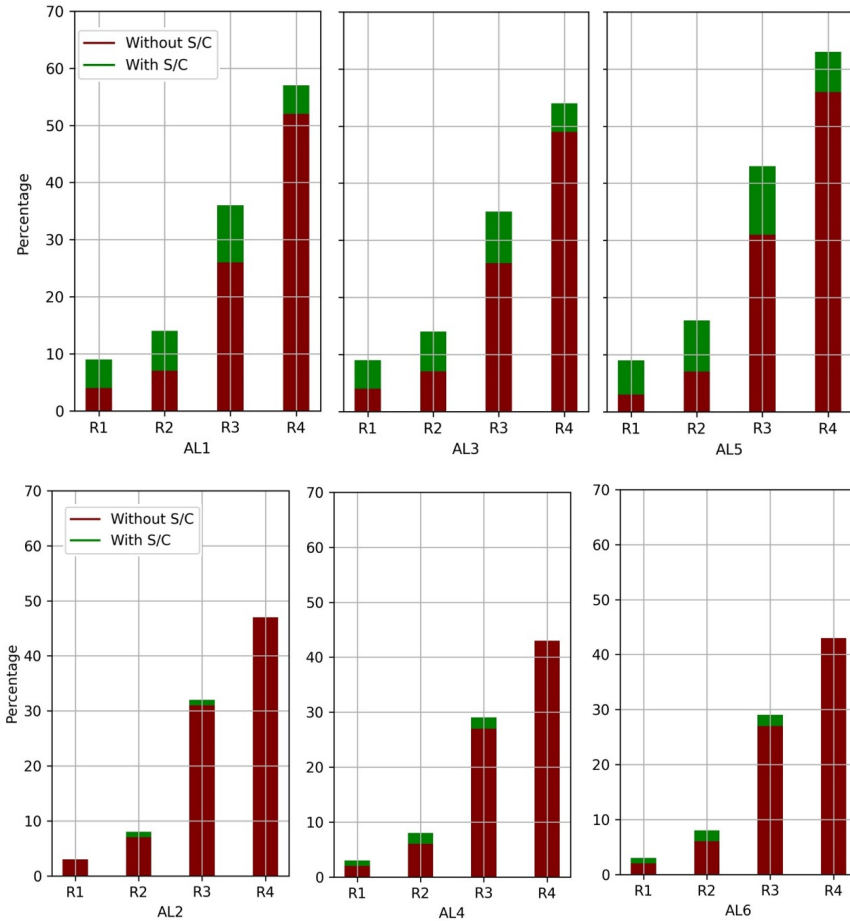


Fig. 15 Improvement in % in libration angles (AL) on the addition of spacecraft with 1-cm accurate range measurement between the s/c and the North Pole LLRR, along with the LLRR range uncertainty assumption sets.

the IAU Working Group on Cartographic Coordinates and Rotational Elements: 2015. *Celestial Mechanics and Dynamical Astronomy* 130(3):22, DOI 10.1007/s10569-017-9805-5

- [2] Damour T, Soffel M, Xu C (1991) General-relativistic celestial mechanics. I. Method and definition of reference systems. *Phys. Rev. D* 43(10):3273–3307, DOI 10.1103/PhysRevD.43.3273
- [3] Fienga A, Laskar J, Morley T, Manche H, Kuchynka P, Le Poncin-Lafitte C, Budnik F, Gastineau M, Somenzi L (2009) INPOP08, a 4-D planetary ephemeris: from asteroid and time-scale computations to ESA Mars Express and Venus Express contributions. *Astron. Astrophys.* 507:1675–1686, DOI 10.1051/0004-6361/200911755, [0906.2860](https://doi.org/10.1051/0004-6361/200911755)
- [4] Fienga A, Deram P, Viswanathan V, Di Ruscio A, Bernus L, Durante D,

- Gastineau M, Laskar J (2019) INPOP19a planetary ephemerides. *Notes Scientifiques et Techniques de l'Institut de Mecanique Celeste* 109
- [5] Fienga A, Deram P, Di Ruscio A, Viswanathan V, Camargo J, Bernus L, Gastineau M, Laskar J (2021) INPOP21a planetary ephemerides. *Notes Scientifiques et Techniques de l'Institut de Mecanique Celeste* 110
- [6] Folkner WM, Williams JG, Boggs DH, Park RS, Kuchynka P (2014) The Planetary and Lunar Ephemerides DE430 and DE431. *Interplanetary Network Progress Report* 196:1–81
- [7] Fuchs MJ, Bouman J (2011) Rotation of GOCE gravity gradients to local frames. *Geophysical Journal International* 187(2):743–753, DOI 10.1111/j.1365-246X.2011.05162.x
- [8] Giordano P, Grenier A, Zoccarato P, Bucci L, Cropp A, Swinden R, Otero D, El-Dali W, Carey W, Duvet L, Hufenbach B, Joly F, Ventura-Traveset J (2021) Moonlight navigation service - how to land on peaks of eternal light
- [9] Iess L, di Benedetto M, Boscagli G, Racioppa P, Sesta A, de Marchi F, Cappuccio P, Durante D, Molli S, Plumaris M, Tartaglia P, Fienga A, Rambaux N, Santi F, Pastina D, Linty N, Sosnica K, Bury G, Zajdel R, Belfi J, Giordano P, Swinden R, Ventura-Traveset J (2024) A novel orbit determination and time synchronization architecture for a radio navigation satellite constellation in the cislunar environment. vol in press
- [10] Konopliv AS, Asmar SW, Carranza E, Sjogren WL, Yuan DN (2001) Recent Gravity Models as a Result of the Lunar Prospector Mission. *Icarus* 150(1):1–18, DOI 10.1006/icar.2000.6573
- [11] Konopliv AS, Park RS, Yuan DN, Asmar SW, Watkins MM, Williams JG, Fahnestock E, Kruizinga G, Paik M, Strelakov D, Harvey N, Smith DE, Zuber MT (2013) The JPL lunar gravity field to spherical harmonic degree 660 from the GRAIL Primary Mission. *Journal of Geophysical Research (Planets)* 118(7):1415–1434, DOI 10.1002/jgre.20097
- [12] Löcher A, Hofmann F, Gläser P, Haase I, Müller J, Kusche J, Oberst J (2017) Towards improved lunar reference frames: Lro orbit determination. In: van Dam T (ed) REFAG 2014, Springer International Publishing, Cham, pp 201–207
- [13] LRO Project and Lunar Geodesy and Cartography Working Group (2008) A Standardized Lunar Coordinate System for the Lunar Reconnaissance Orbiter and Lunar Datasets: LRO Project and LGCWG White Paper. Tech. rep.
- [14] Mazarico E, Rowlands DD, Neumann GA, Smith DE, Torrence MH, Lemoine FG, Zuber MT (2012) Orbit determination of the Lunar Reconnaissance Orbiter. *Journal of Geodesy* 86(3):193–207, DOI 10.1007/s00190-011-0509-4
- [15] Nelson R, Ely T (2006) Relativistic transformations for time synchronization and dissemination in the solar system
- [16] Oberst J, Haase I, Glaser P (2019) Verbesserung und Verdichtung des LOLA Mondkontrollpunkt-netzes durch LROC/LOLA-Blochausgleiche und Landstellenanalysen anhand von DGM und Karten. Tech. rep., TUB Förderkennzeichen 50 OW1702
- [17] Park RS, Folkner WM, Williams JG, Boggs DH (2021) The JPL Planetary and Lunar Ephemerides DE440 and DE441. *Astron. J* 161(3):105, DOI 10.3847/

- 1538-3881/abd414
- [18] Pavlov D (2020) Role of lunar laser ranging in realization of terrestrial, lunar, and ephemeris reference frames. *Journal of Geodesy* 94(1):5, DOI 10.1007/s00190-019-01333-y, [1911.08235](https://doi.org/10.1007/s00190-019-01333-y)
 - [19] Petit G, Luzum B (2010) IERS Conventions (2010). IERS Technical Note 36:1
 - [20] Rambaux N, Williams JG (2011) The Moon's physical librations and determination of their free modes. *Celestial Mechanics and Dynamical Astronomy* 109(1):85–100, DOI 10.1007/s10569-010-9314-2
 - [21] Soffel M (2003) The IAU 2000 Resolutions for Astrometry, Celestial Mechanics, and Metrology in the Relativistic Framework: Explanatory Supplement. *Astronomical Journal* 126:2686–2706
 - [22] Tapley B, Schutz B, Born G (2004) *Statistical Orbit Determination*. Elsevier
 - [23] Turyshev SG, Toth VT, Sazhin MV (2013) General relativistic observables of the GRAIL mission. *Phys. Rev. D* 87(2):024020, DOI 10.1103/PhysRevD.87.024020, [1212.0232](https://doi.org/10.1103/PhysRevD.87.024020)
 - [24] Viswanathan V (2017) Improving the dynamical model of the moon using lunar laser ranging (LLR) and spacecraft data. PhD thesis, Observatoire de Paris, URL <https://theses.hal.science/tel-01792665>
 - [25] Viswanathan V, Fienga A, Minazzoli O, Bernus L, Laskar J, Gastineau M (2018) The new lunar ephemeris INPOP17a and its application to fundamental physics. *Mon. Not. R. Astron. Soc.* DOI 10.1093/mnras/sty096, [1710.09167](https://doi.org/10.1093/mnras/sty096)
 - [26] Viswanathan V, Rambaux N, Fienga A, Laskar J, Gastineau M (2019) Observational Constraint on the Radius and Oblateness of the Lunar Core-Mantle Boundary. *Geophys. Res. Lett.* 46(13):7295–7303, DOI 10.1029/2019GL082677, [1903.07205](https://doi.org/10.1029/2019GL082677)
 - [27] Williams JG, Boggs DH (2008) DE421 lunar orbit, physical librations, and surface coordinates. Tech. rep., jPL Interoffice Memorandum IOM 335-JW
 - [28] Williams JG, Boggs DH (2021) Testing the Motion of Lunar Retroreflectors. *Journal of Geophysical Research (Planets)* 126(11):e06920, DOI 10.1029/2021JE006920
 - [29] Williams JG, Boggs DH, Currie DG (2022) Next-generation Laser Ranging at Lunar Geophysical Network and Commercial Lander Payload Service Sites. *The Planetary Science Journal* 3(6):136, DOI 10.3847/PSJ/ac6c25